Journal of Materials Science & Technology 122 (2022) 128–140

Contents lists available at ScienceDirect

Journal of Materials Science & Technology

journal homepage: www.elsevier.com/locate/jmst

Research Article

# High-temperature failure mechanism and defect sensitivity of TC17 titanium alloy in high cycle fatigue

Gen Li[a], Chengqi Sun[a,b,*]

[a] State Key Laboratory of Nonlinear Mechanics, Institute of Mechanics, Chinese Academy of Sciences, Beijing 100190, China
[b] School of Engineering Science, University of Chinese Academy of Sciences, Beijing 100049, China

ARTICLE INFO

*Article history:*
Received 14 December 2021
Revised 4 January 2022
Accepted 4 January 2022
Available online 20 March 2022

*Keywords:*
TC17 titanium alloy
High temperature
Defect
High cycle fatigue
Oxygen-rich layer
Rough area

ABSTRACT

Crack initiation is an essential stage of fatigue process due to its direct effect on fatigue failure. However, for titanium alloys in high-temperature high cycle fatigue (HCF), the crack initiation mechanisms remain unclear and the understanding for the defect sensitivity is also lacking. In this study, a series of fatigue tests and multi-scale microstructure characterizations were conducted to explore the high-temperature failure mechanism, and the coupled effect of temperature and defect on TC17 titanium alloy in HCF. It was found that an oxygen-rich layer (ORL) was produced at specimen surface at elevated temperatures, and brittle fracture of ORL at surface played a critical role for surface crack initiation in HCF. Besides, internal crack initiation with nanograins at high temperatures was a novel finding for the titanium alloy. Based on energy dispersive spectroscopy, electron backscatter diffraction and transmission electron microscope characterizations, the competition between surface and internal crack initiations at high temperatures was related to ORL at surface and dislocation resistance in inner microstructure. The fatigue strengths of smooth specimens decreased at elevated temperatures due to the lower dislocation resistance. While the fatigue strengths of the specimens with defect were not very sensitive to the temperatures. Finally, a fatigue strength model considering the coupled effect of temperature and defect was proposed for TC17 titanium alloy.



## 1. Introduction

Titanium alloys are widely used in aero engines due to their excellent mechanical properties, lightweight, high temperature resistance and high corrosion resistance. Some of the components, such as compressor blisks and blades, work in a high-temperature environment and are subject to high cycle fatigue (HCF, $10^5$-$10^7$) and very high cycle fatigue (VHCF, $>10^7$) loadings. Therefore, fully understanding the high-temperature fatigue behavior and failure mechanism of titanium alloys in HCF and VHCF regimes are of great importance for flight safety and reliability.

Existing studies of high-temperature fatigue of titanium alloys [1–4] found that oxygen diffused around surface and subsurface of tested specimens at elevated temperatures, which could produce a hardened and brittle oxygen-rich layer (ORL). Satko et al [2]. investigated oxygen ingress behavior for a near $\alpha$ titanium alloy at 650 °C with various microstructures and reported that basketweave microstructure had the best resistance to high-temperature oxidation and the highest crack nucleation strain. The capacities of equiaxed and bimodal microstructures were weaker and colony microstructure had the lowest resistance to the oxidation. Such a brittle ORL reduced the crack nucleation strain [2] and was harmful to the low cycle fatigue (LCF, $<10^5$ cycles) behavior due to a relatively larger stress amplitude in LCF. Brittle fracture of the oxygen-rich site became a major failure mode in LCF of titanium alloys at high temperatures [1, 5, 6]. Although numerous studies have been reported for the high-temperature fatigue of titanium alloys and the effect of ORL, most of them worked on LCF behavior [1, 5-13], and the related studies for HCF and VHCF tests at high temperatures were limited [3, 4, 14, 15]. Meanwhile, these studies mainly focused on the temperature effect on the fatigue behavior, but less on the failure mechanisms. It was found that elevated temperatures in HCF and VHCF tests could lead to brittle fracture of ORL [3, 4], accelerate the crack growth behavior [3, 14, 16, 17] and weaken the fatigue strength [3, 4, 14]. Unlike the limited understanding at high temperatures, the failure mechanisms at room temperature have been widely investigated [18–26]. Surface crack initiation was commonly viewed in HCF tests, and with a decrease

* Corresponding author
*E-mail address:* scq@lnm.imech.ac.cn (C. Sun).

https://doi.org/10.1016/j.jmst.2022.01.010
1005-0302/

of stress amplitude, internal crack initiation could compete with surface crack initiation in HCF and VHCF regimes [19, 21, 22]. In some cases, the internal crack initiation presented a rough area with local refined grains [19, 27], which was caused by dislocation interaction due to high strain localization in the microstructure and then originating microcracks within the nanograins or along the boundary of nanograin and coarse grain [27]. Therefore, there is a research gap to be explored in the high-temperature situation.

Moreover, the titanium-alloy structures may contain surface defects in manufacturing process or long-term usage, which can reduce their fatigue lifetime and accelerate structural failure. A clear understanding of the coupled effect of high temperature and defect on the fatigue behavior of titanium alloys is important. However, numerous studies for the effect of defects on titanium alloys are at room temperature [28–32] and the studies at high temperatures are quite limited [33]. Nazmy et al. [33] tested specimens of titanium alloy with a notch defect at 700 °C and 750 °C in HCF regime, but they did not compare the results with those at room temperature. Therefore, it is necessary to elucidate the effect of defect on titanium alloys at elevated temperatures in HCF and VHCF and establish a fatigue strength model for these scenarios.

The current study aimed to explore the high-temperature failure mechanism, and the coupled effect of high temperature and surface defect on TC17 titanium alloy in HCF regime. TC17 titanium alloy with basketweave microstructure is commonly used for compressor components in aero engines and it was selected in this study. A series of fatigue tests for smooth specimens and notched specimens were conducted at room and high temperatures. Effects of high temperature and defect on the S-N data and failure modes were examined and discussed in detail. To understand the failure mechanisms, the crack initiation sites were investigated by multiscale microstructure characterization with a scanning electron microscope (SEM) and a transmission electron microscope (TEM). The crack behaviors of TC17 alloy were studied via SEM and electron backscatter diffraction (EBSD). A fatigue strength model was proposed for smooth and notched specimens at different temperatures. The results and analysis could be helpful in the engineering design of TC17 alloy for compressor components and provide a reference for the high-temperature fatigue mechanism of titanium alloys.

## 2. Experimental program

### 2.1. Material and microstructure

The TC17 titanium alloy used in this study was received as a solid bar. The heat treatment process of this material started from beta forging, followed by solid solution at 800 °C for 4 h and water cooling. After that, the material was under aging treatment at 620 °C for 8 h and then air cooling. The chemical composition is 4.97 Al, 4.19 Cr, 1.90 Zr, 4.12 Mo, 2.09 Sn, 0.11 O, <0.10 Fe, 0.0052 H, 0.004 C and balanced Ti in mass percent. The TC17 alloy owns a basketweave microstructure, as shown in Fig. 1(a-d). Fig. 1(a) shows the band contrast map observed by a field emission scanning electron microscope (FE-SEM), and $\alpha$ phase and $\beta$ phase have volume fractions of 0.692 and 0.276, respectively. Fig. 1(b-d) shows the EBSD derived inverse pole figures (IPFs). A large $\alpha$ cluster and anisotropic $\alpha$ grains are shown in Fig. 1(c) and 1(d), respectively. The grain sizes in TC17 alloy are not uniform.

Due to the interest of the microstructure around the surface defect (i.e., small notch), a notched specimen was cut by a saw along the axis of the specimen and the direction is perpendicular to the notch. Its sectional view is presented in Fig. 1(e), including a phase map and an IPF. The notch on specimens were fabricated by wire electrical discharge machining (WEDM). It removed the material by spark erosion and the microstructure around the notch was seriously damaged. Fig. 1(e) and (f) show that the coarse surface of

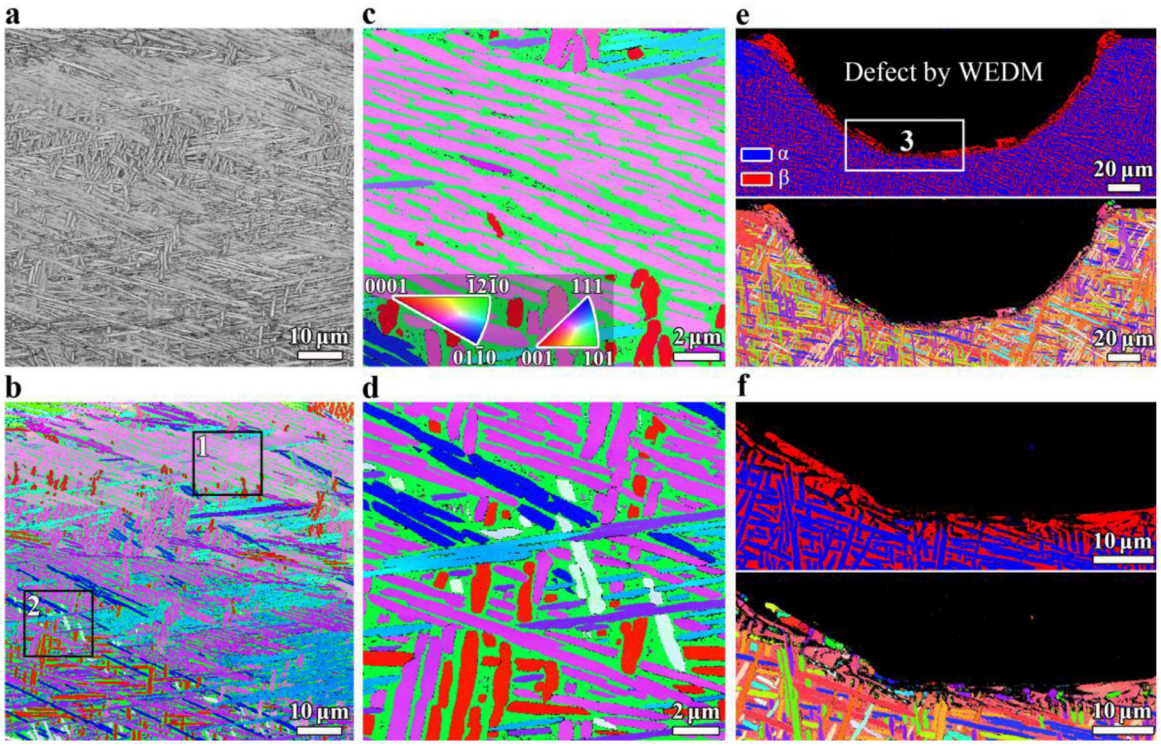


**Fig. 1.** EBSD microstructural characterization of TC17 titanium alloy. (a, b) Band contrast map and IPF. (c, d) Enlarged view of box 1 and 2 in (b), respectively, showing $\alpha$ cluster and anisotropic $\alpha$ grains. Inset in (c) the color legend for IPF. (e) Phase map (upper part) and IPF (lower part) near the defect. (f) Enlarged view of phase map (upper part) and IPF (lower part) of box 3 in (e).

**Table 1**
Mechanical properties of TC17 alloy.

| Temperature (°C) | Elastic modulus (GPa) | Yield strength (MPa) | Tensile strength (MPa) | Elongation to failure (%) |
|---|---|---|---|---|
| 25 | 118 | 1047 | 1141 | 11.9 |
| 200 | 112 | 920 | 1054 | 11.3 |
| 400 | 103 | 735 | 912 | 12.1 |

the notch is an irregular layer of $\beta$ phase in a depth of around 5 μm. The WEDM erodes the original $\alpha$ phase in this layer.

Considering a working environment of room temperature to 400 °C for TC17 alloy in jet engines, testing temperatures of 25 °C, 200 °C and 400 °C were selected for quasi-static tensile tests to provide the mechanical properties of the alloy. Three cylindrical specimens with gauge length of 30 mm and diameter of 5 mm were tested at each temperature by a servo-hydraulic test system. The strain was measured with an extensometer of 25 mm, and the strain rate was $10^{-4}$ $s^{-1}$. The detailed properties are given in Table 1. This material presented yield strength $\sigma_{ys}$ of 735 MPa and tensile strength $\sigma_{ts}$ of 912 MPa at a high temperature of 400 °C. It was found that the elastic modulus, yield strength and tensile strength decreased with an increase in temperature, which indicated relatively weaker mechanical properties at 400 °C. The elongation to failure was in a range of 11.3% to 12.1%, which did not show a large variation at 25 °C, 200 °C and 400 °C.

### 2.2. Test methods

According to fatigue test standard ASTM E466 [34], hourglass-shaped specimens with a minimum diameter of 5 mm were machined out from the TC17 alloy bar. A radius curvature of 50 mm was designed for the arc transition zone to minimize stress concentration. The surface of the hourglass part of the smooth specimen was polished to a mirror finish before the tests to eliminate the effect of surface scratches. To study the sensitivity of TC17 alloy to various defect sizes, small notches perpendicular to the axis of the specimen were fabricated on the minimum section of the polished smooth specimens by WEDM with a round wire of 0.2 mm diameter. The notches were 0.05 mm, 0.2 mm and 0.5 mm in depths.

The fatigue tests were conducted on high-frequency fatigue machines made by Sinotest and MTS with a stress ratio ($R$) of -1 in air. The loading frequencies were in a range of 80 to 110 Hz. To examine the effect of temperature on the smooth and notched specimens, the fatigue behavior of TC17 alloy at 25 °C, 200 °C and 400 °C was investigated. At 25 °C and 200 °C, the fatigue tests were conducted for smooth specimens and notched specimens with all three notch depths (0.05 mm, 0.2 mm and 0.5 mm). Followed by the tests at 400 °C, smooth specimens and specimens with notch depths of 0.05 mm and 0.5 mm were examined. After the fatigue tests, the hardness values of the specimen surface at 25 °C, 200 °C and 400 °C were measured for the study of surface oxidation. Specimens at each temperature were chosen and 4 mm long cylinders at the minimum section of the specimens were cut out. Ten points were tested on the surface for each specimen using a microhardness tester with a load of 50 gf and holding time of 15 s. Besides, the hardness of the subsurface material was also tested using the same method on cross sections of several run-out specimens tested at different temperatures. The cross sections were cut out near the minimum section of the specimens and were polished carefully.

### 2.3. Fractography observation

After the fatigue tests, the fracture surfaces of the failed specimens were observed by a SEM. The oxygen-rich layer for the specimens at high temperatures was analyzed by energy dispersive spectroscopy (EDS) on Zeiss GeminiSEM 300. For some specimens failed by internal crack initiation, a slice in the initiation area was extracted by focused ion beam (FIB) along the loading direction and then was observed by FEI Tecnai G20 TEM. Some run-out notched specimens were cut along the loading direction to investigate the damage behaviors at the notch root. These sections were polished carefully in a mirror finish and were characterized by EBSD on Nordlys of Oxford Instruments.

## 3. Results and discussion

### 3.1. Fatigue strength and fatigue life

The S-N data of the tested specimens are shown in Fig. 2. The stress amplitudes in this study are nominal stress amplitude and they are calculated by the smallest net section. Run out represents to stop loading if fatigue life is over 2.0 (or 5.0) $\times$ $10^7$ cycles and such samples are marked by arrows. Best-fit lines are determined by least square method [35] and are shown in Fig. 2 to indicate the general tendencies of each configuration. The fatigue strengths at 2.0 $\times$ $10^7$ cycles in this study are determined by the fitting line. Before the regression work, an estimated fatigue strength is determined by an average value of the maximum stress amplitude among the run-out specimens and the minimum stress amplitude among the failed specimens. The run-out specimens tested with stress amplitude 5% lower than the estimated fatigue strength is not considered in the regression. The smooth specimens at 25 °C in Fig. 2(a) reach a high cycle fatigue regime ($>10^5$ cycles) at a stress amplitude of 650 MPa and present a fatigue strength of 629 MPa with a platform. With an increase in temperature, the platform is disappeared, and the fatigue strengths of the smooth specimens decrease continuously, from 629 MPa at 25 °C to 416 MPa at 400 °C. The fatigue strengths ($\sigma_{fs}$) and the tensile strength ($\sigma_{ts}$) at elevated temperatures are compared in Fig. 2(b). Both strength values decrease with an increase of temperature, and the decreasing gradients of the tensile strength and the fatigue strength are close. This trend is also noticed for the TC17 alloy with bimodal microstructure [4] and the effect of temperature could be contributed to a decrease of the resistance to the dislocation movement of TC17 alloy at high temperatures [4]. The values of fatigue strengths and tensile strength are given in Table 2. In fatigue research, a fatigue ratio of $\frac{\sigma_{fs}}{\sigma_{ts}}$ is used to evaluate the relation between fatigue strength and tensile strength. The strength ratios summarized in Table 2 are distributed in a range of 0.46 to 0.55, which means that the ratios at high temperatures are consistent with those at room temperature [36].

**Table 2**
Tensile strength and fatigue strength of the TC17 alloys.

| Tests | Temperature (°C) | $\sigma_{ts}$ (MPa) | $\sigma_{fs}$ (MPa) | $\frac{\sigma_{fs}}{\sigma_{ts}}$ |
|---|---|---|---|---|
| Current | 25 | 1141 | 629 | 0.55 |
| | 200 | 1054 | 530 | 0.50 |
| | 400 | 912 | 416 | 0.46 |
| Liu et al [4] | 25* | 1078 | 530 | 0.49 |
| | 400 | 853 | 450 | 0.53 |

*It denotes room temperature in literature.

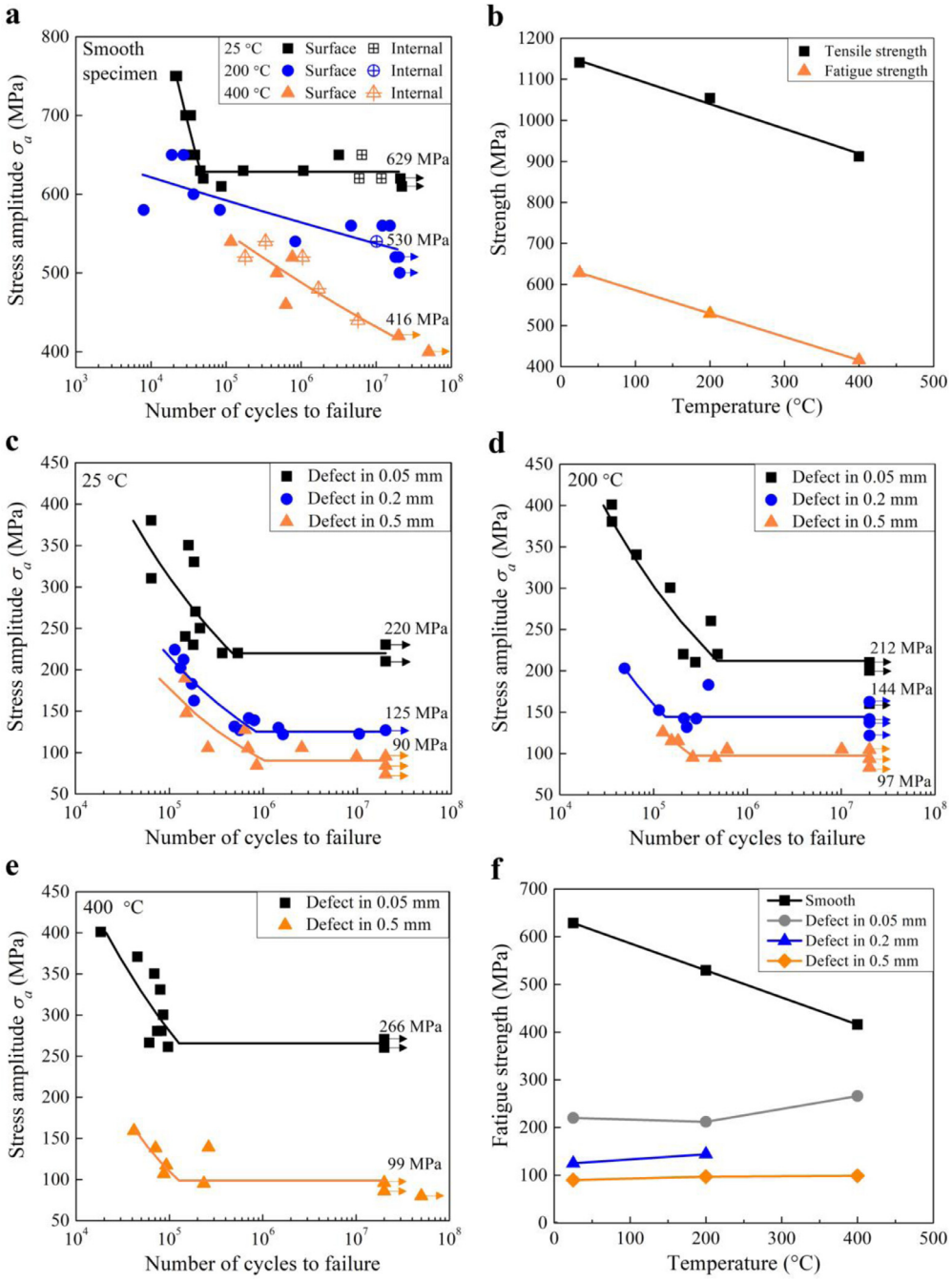


**Fig. 2.** Test results: (a) S-N data of smooth specimens tested at 25 °C, 200 °C and 400 °C. (b) Variation of fatigue strengths and tensile strengths of smooth specimens with temperatures. (c)-(e) S-N data of notched specimens at 25 °C, 200 °C and 400 °C, respectively. (f) Variation of fatigue strengths of smooth and notched specimens with temperatures.

Surface and internal crack initiation modes at different temperatures are also presented in Fig. 2(a). At 25 °C and 200 °C, surface crack initiation was a dominant failure mode for most specimens and internal crack initiation only happened for the specimens failed at around $10^7$ cycles. These results were similar to those room-temperature fatigue studies of titanium alloys [19, 27]. However, different from the cases at 25 °C and 200 °C, internal crack initiation occurred for some specimens with much shorter fatigue lives ($10^5$-$10^6$ cycles) at 400 °C. This was a new finding for titanium alloy at high temperature in HCF regime, which indicated a different failure mechanism. The fracture morphologies and the failure mechanisms are presented and discussed in Sections 3.2 and 3.3.

The S-N curves of the specimens with different notch depths at 25 °C, 200 °C and 400 °C are shown in Fig. 2(c-e), respectively. The variation of the fatigue strengths of smooth and notched specimens with temperatures is presented in Fig. 2(f). Due to the effect of surface defect, the stress amplitudes of the notched specimens in all the three notch depths in Fig. 2(c-e) are significantly lower than those of smooth specimens in Fig. 2(a). Besides, the S-N curves by the best-fit lines of these notched specimens present platforms. In terms of the notched specimens at 25 °C in Fig. 2(c), the fatigue strengths decrease continuously with larger notch depths and the results are 220 MPa, 125 MPa and 90 MPa for specimens with notch depths of 0.05 mm, 0.2 mm and 0.5 mm, respectively. It indicated that the larger defect led to the lower fa-

tigue strength. The notched specimens at 200 °C in Fig. 2(d) show similar fatigue strengths with those at 25 °C for the specimens with all the three notch depths. The results revealed that the environmental temperature at 200 °C did not have an obvious effect on the fatigue strength of the notched specimens. However, at 400 °C in Fig. 2(e) and (f), the fatigue strength of notched specimens in 0.05 mm is 266 MPa, which is higher than those at the other temperatures. The notched specimens in depth of 0.5 mm own a fatigue strength of 99 MPa at 400 °C, which is close to the other two configurations. This interesting difference might be attributed to surface hardening by ORL formed at 400 °C, which is explained in Section 3.3.1. For the specimens with a shallow notch, the hardened oxide at the notch root could restrain crack nucleation and improve the fatigue strength. When the notch was deeper, due to the higher stress concentration at the notch root, the influence of the hardened oxide layer became weaker and the notch dominated the fatigue strength.

### 3.2. SEM observation of fracture surface

#### 3.2.1. Smooth specimens at room temperature

Fig. 3 shows fracture surface morphologies of smooth specimens, including surface and internal crack initiation modes. A typical surface crack initiation of a specimen tested at 25 °C is shown in Fig. 3(a1-a3). The sample was tested with an amplitude of 650 MPa and failed at a fatigue life of $3.9 \times 10^4$ cycles. The crack initiation site indicates a facet with $\alpha$ clusters in quasi-plane orientation in Fig. 3(a2) and (a3), which suggests cleavage of $\alpha$ grains under the cyclic loadings.

Fig. 3(b1-b3) shows a sample tested at 620 MPa at 25 °C and failed by internal crack initiation. The initiation site in Fig. 3(b1) and (b2) is a rough area and is surrounded by ridge patterns. The fracture morphology is similar to the internal crack initiation of titanium alloys observed at room temperature in literature [4, 19, 21]. Different from the regular small facets in rough area for equiaxial and bimodal microstructures in literature [4, 37], the facet feature is not observed in the rough area for the present TC17 alloy, as shown in Fig. 3(b3).

#### 3.2.2. Smooth specimens at high temperatures

Fig. 3(c1-c3) presents the fracture surface morphology of a sample tested at 650 MPa and 200 °C and failed at $2.7 \times 10^4$ cycles. Two surface crack initiation sites are found for this specimen and, due to intersection of the two cracks, undulating ridges are formed between them. Fig. 3(c2) and (c3) show the enlarged views of the two crack initiation sites, respectively. The oxidation traces are observed along the edge of the fracture surface in Fig. 3(c2). This could be due to that oxygen diffused into the subsurface during the testing process and formed an oxide layer (i.e. ORL). The break of oxide layer would cause stress concentration and crack nucleation. The failure mode due to oxygen intrusion was also observed for TC17 alloy with bimodal microstructure at 400 °C [4]. Fig. 3(d1-d4) shows a different mechanism of surface crack initiation from Fig. 3(c1-c3). The sample was tested at 520 MPa and 400 °C and failed at $7.6 \times 10^5$ cycles. The surface oxide layer is noticed in Fig. 3(d2), and it is brittle and could shed during the cyclic loadings. As shown in Fig. 3(d3) and (d4), the shedding locations are found at the crack initiation site, and the crack could nucleate at this site due to the stress concentration after shedding. Subsequently, the crack extended to the internal area of the specimen. Fig. 3(c1-c3) and (d1-d4) present the failure modes of oxygen intrusion and oxide shedding at elevated temperatures in air, respectively, and both surface crack modes were found in the specimens tested at 200 °C and 400 °C.

After the discussion of surface crack initiation at high temperatures, a special failure mode, i.e., internal crack initiation at 400 °C, is presented in Fig. 3(e1-e3). The crack initiation region in Fig. 3(e1-e3) exhibits a rough area, which is similar to that for the internal crack initiation at 25 °C. Since the specimens shown in Fig. 3(d1-d4) and (e1-e3) were loaded with a same stress amplitude of 520 MPa, the different failure modes between Fig. 3(d1-d4) and (e1-e3) indicated a competition mechanism between surface and internal crack initiations in HCF regime at 400 °C. Some studies on nickel-based superalloys and steels [38–41] have reported the competition mechanism between surface crack initiation and internal crack initiation at high temperatures. They found that the ORL tended to fracture and initiate cracks at the surface under high stress amplitudes, but at low stress amplitudes, the crack nucleation could occur at internal inclusions or defects. Since titanium alloys normally do not contain inclusions and defects, the internal $\alpha$ grain clusters and large $\alpha$ grains become potential crack initiation sites when the surface crack initiation is suppressed.

#### 3.2.3. Notched specimens at room and high temperatures

Unlike the smooth specimens, the fatigue crack of the failed notched specimens all initiated from the notch root due to the stress concentration. Fig. 4 shows the fracture surface morphologies of the notched specimens at different temperatures. Some tiny pores and roughness are found at the notch root of the specimens at 25 °C, 200 °C and 400 °C, as shown in Fig. 4(a3), (b2), (b3) and (c2). They are consistent with the microstructure characteristics around the notch in Fig. 1(e) and (f). The pores and roughness promoted the crack initiation at the notch root due to the local stress concentration, and reduced the fatigue strengths of the notched specimens. Additionally, the oxide is also observed at the notch root of the specimens tested at 400 °C, as shown in Fig. 4(c3).

### 3.3. Crack initiation mechanism

#### 3.3.1. Oxygen-rich layer at high-temperature fatigue tests

To study the effect of holding time on the ORL at high temperatures, the hardness of specimen surface with different holding times at 25 °C, 200 °C and 400 °C was measured by a microhardness tester. The selected specimens owned fatigue cycles in a range from $8.3 \times 10^4$ to $2.0 \times 10^7$, and the holding time was in a range of 0.2 to 50 h which was obtained by dividing the fatigue life by the testing frequency. The heating time for 200 °C and 400 °C before fatigue tests was about 0.5 h, and it was not included in the holding time. The hardness values versus holding time are shown in Fig. 5(a), and error bars in the figure indicate standard deviations of the hardness. It was found that the hardness showed a slight increase trend with a longer holding time for both 200 °C and 400 °C. The hardness values of the specimens tested at 200 °C were similar with those at 25 °C for a shorter holding time (e.g., 0.2-2.4 h), while the values at 200 °C were slightly higher for a longer holding time (~50 h). However, the hardness range at 400 °C was significantly higher than that at 200 °C even for the short holding time (e.g., 0.28 h). The mean hardness for the holding time of 0.28 h ($1.2 \times 10^5$ cycles) at 400 °C was 502 HV, which was 19.3% higher than the mean hardness for the holding time of about 50 h ($2.0 \times 10^7$ cycles) at 200 °C. These results indicated that the action of the ORL on the fatigue behavior at 400 °C started at very small loading cycles (~$10^5$ cycles). The hard ORL formed at 400 °C could restrain the surface crack initiation and benefit a longer fatigue life. It agreed with the finding in Fig. 2(a) that the internal crack initiation was popular for the specimen with a fatigue life in the range of $10^5$ to $10^7$ cycles at 400 °C.

The hardness of the subsurface material was also measured to understand the oxygen ingress behavior. The run-out specimens at each temperature were selected due to their longest exposure time at elevated temperatures. As the microhardness tester produced an indentation with a diagonal length of about 7 $\mu$m in this study,

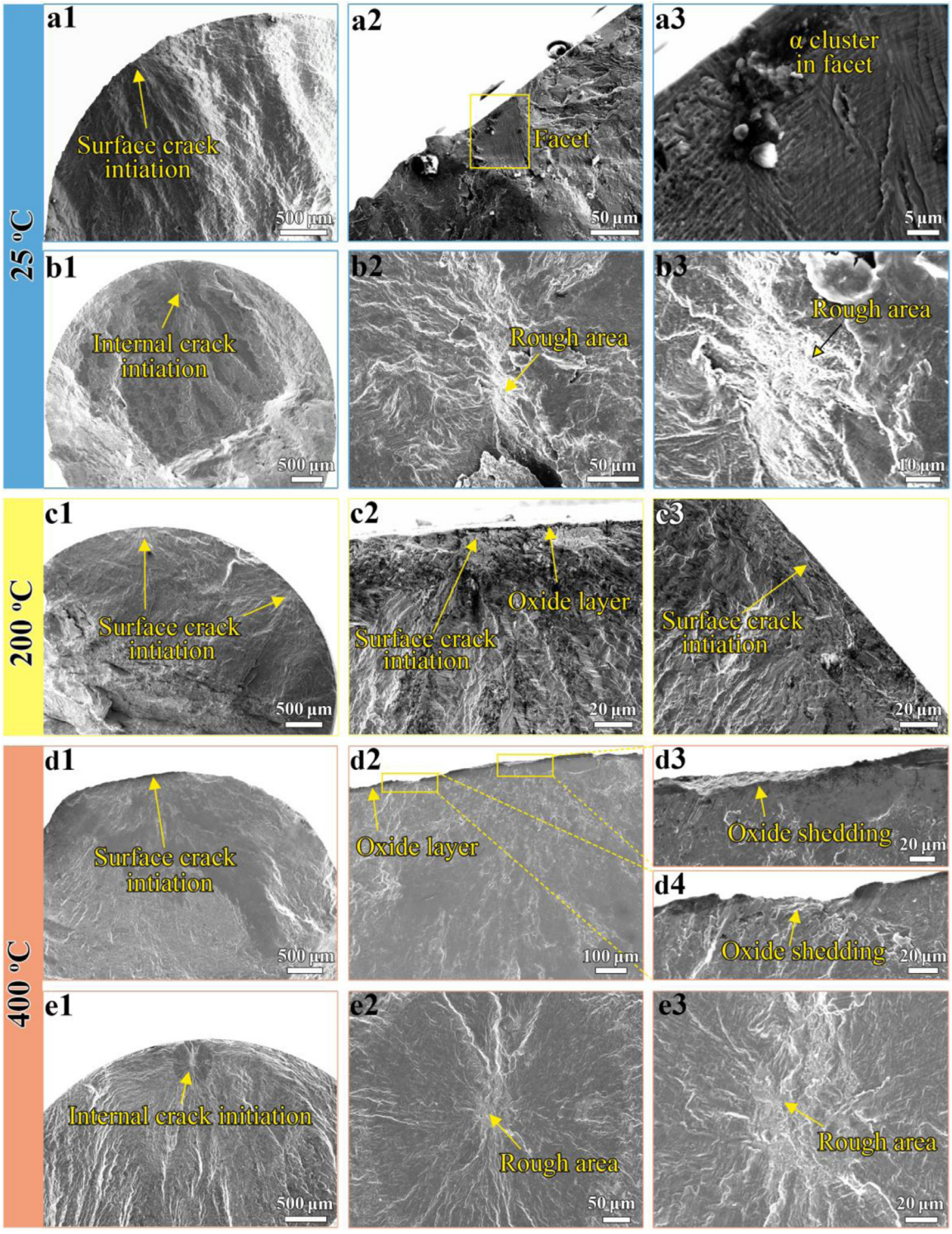


**Fig. 3.** Fracture surfaces of smooth specimens at different temperatures. (a1) Surface crack initiation at 25 °C ($\sigma_a$=650 MPa, $N_f$=3.9 × $10^4$ cycles). (a2) Surface crack initiation with facet. (a3) An enlarged view of the facet in (a2). (b1) Internal crack initiation at 25 °C ($\sigma_a$=620 MPa, $N_f$=6.0 × $10^6$ cycles). (b2) Internal crack initiation with rough area. (b3) An enlarged view of the rough area in (b2). (c1) Multiple surface crack initiations by oxide intrusion at 200 °C ($\sigma_a$=650 MPa, $N_f$=2.7 × $10^4$ cycles). (c2, c3) Close-ups of the upper and the right crack initiation regions in (c1), respectively. (d1) Surface crack initiation by oxide shedding at 400 °C ($\sigma_a$=520 MPa, $N_f$=7.6 × $10^5$ cycles). (d2) An enlarged view of crack initiation region in (d1). (d3, d4) Close-ups of the oxide shedding regions in (d2). (e1) Internal crack initiation at 400 °C ($\sigma_a$=520 MPa, $N_f$=1.0 × $10^6$ cycles). (e2) Internal crack initiation with rough area. (e3) An enlarged view of the rough area in (e2).

the depth from the surface to the center of indentation no less than 10 $\mu$m was tested by the microhardness tester. The sketch for the hardness test and the hardness values at different depths are shown in Fig. 5(b). The hardness values of the surface at 25 °C in Fig. 5(a) and in depth of 45 $\mu$m at 25 °C are provided in Fig. 5(b) for reference. It was found that the hardness values of subsurface material at 200 °C and 400 °C were similar with those at 25 °C, which were around 390 HV. This finding indicated that the depths of oxygen ingress under 200 °C and 400 °C were very thin, which were less than 10 $\mu$m.

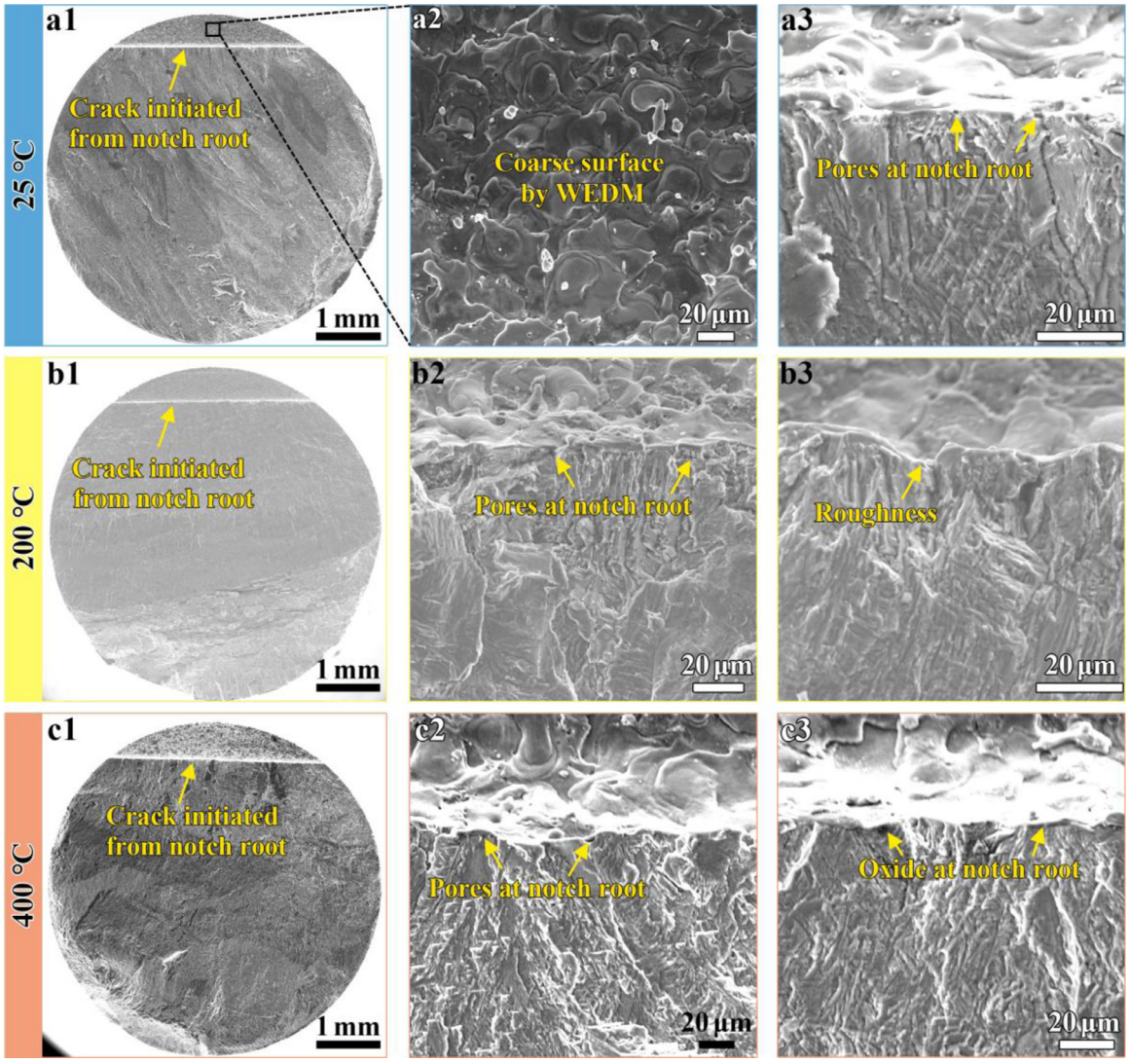


**Fig. 4.** SEM observation of fracture surface of notched specimens at different temperatures. (a1) The whole fracture surface at 25 °C ($\sigma_a$=105 MPa, $N_f$=2.6 × $10^5$ cycles). (a2) A close-up of the coarse surface in black box in (a1). (a3) A close-up of crack initiation zone at notch root in (a1). (b1) The whole fracture surface at 200 °C ($\sigma_a$=95 MPa, $N_f$=4.5 × $10^5$ cycles). (b2) and (b3) Close-ups of crack initiation zone at notch root in (b1). (c1) The whole fracture surface at 400 °C ($\sigma_a$=107 MPa, $N$=8.7 × $10^4$ cycles). (c2, c3) Close-ups of crack initiation zone at notch root in (c1).

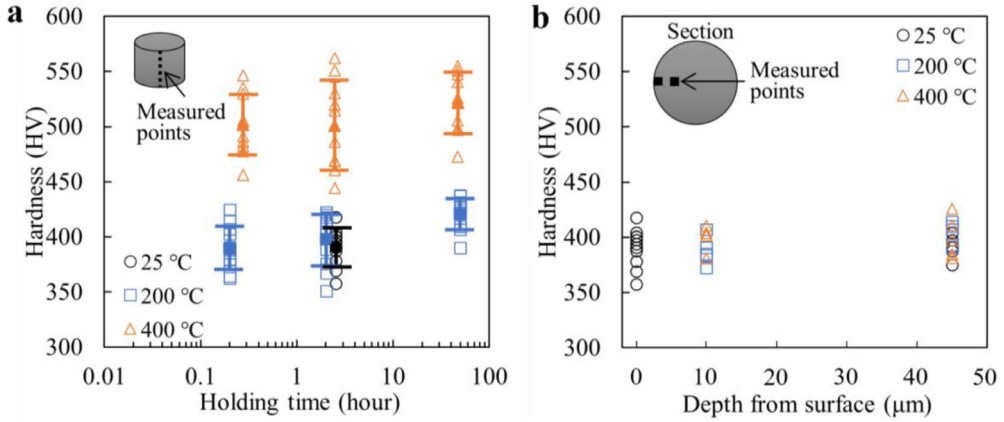


**Fig. 5.** Variation of hardness of the specimens at different temperatures. (a) Hardness values of specimen surface versus holding time. (b) Hardness versus depth from surface on the cross section of run-out specimens at different temperatures. Inset in (a) and (b) the sketches for the hardness tests.

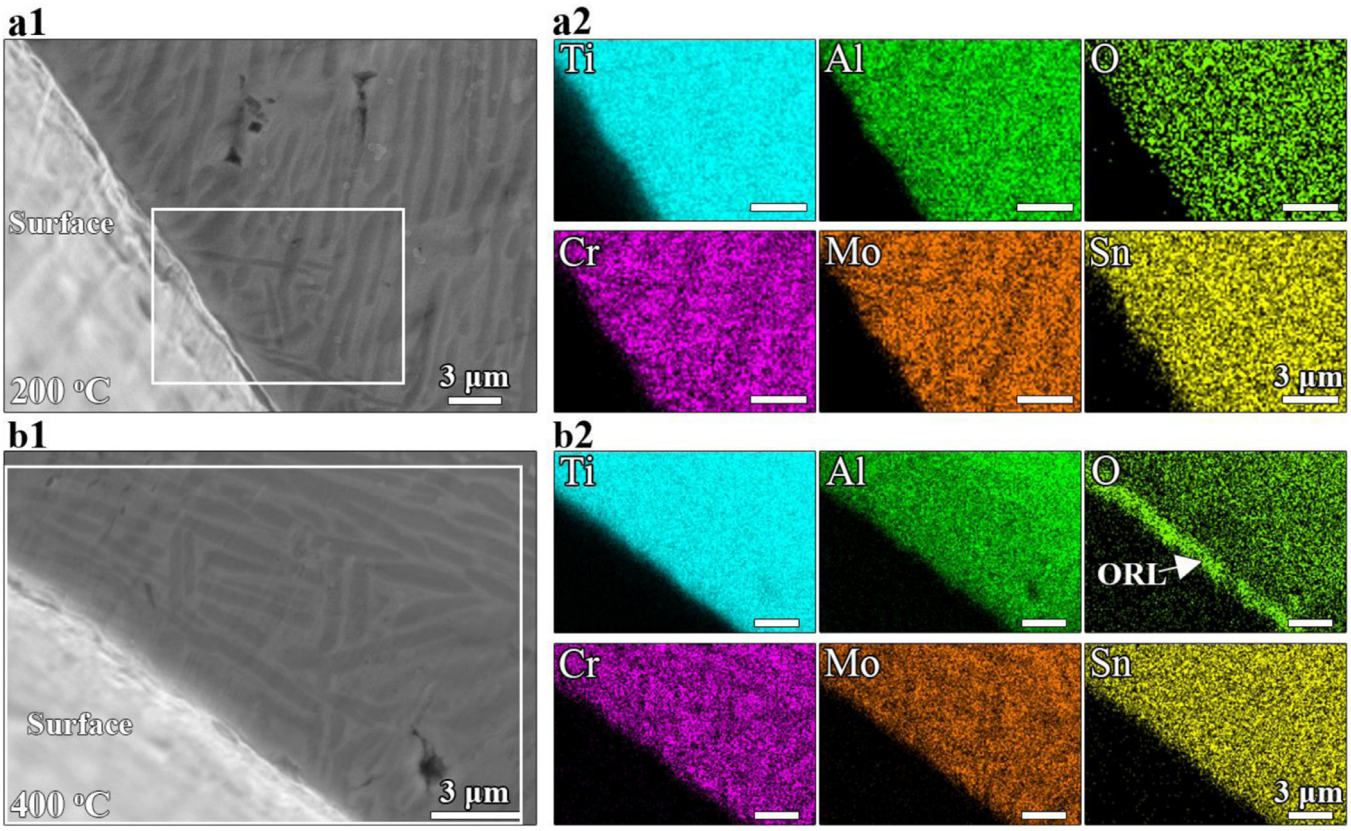


**Fig. 6.** Analysis of ORL by EDS. (a1) SEM image of a section on the specimen tested at 200 °C ($\sigma_a$=540 MPa, $N_f$=8.4 × $10^5$ cycles). (b1) SEM image of a section on the specimen tested at 400 °C ($\sigma_a$=460 MPa, $N_f$=6.2 × $10^5$ cycles). (a2) and (b2) EDS maps of the selected zones in (a1) and (b1), respectively.

To further investigate the property of the ORL formed at high temperatures, EDS was used to analyze oxygen distribution near the specimen surface. The sections of specimens tested at 200 °C and 400 °C are shown in Fig. 6(a1) and (b1), respectively. The associated EDS maps are shown in Fig. 6(a2) and (b2), respectively. In Fig. 6(a2), oxygen element is uniformly distributed from surface to interior, which indicates a lower degree of oxidation at 200 °C. This result is consistent with the finding in Fig. 5(a) that the hardness of specimen surface at 200 °C is close to that at 25 °C. The specimen surface for the tests at 400 °C have experienced severe oxidation. The oxygen element in Fig. 6(b2) is concentrated at the surface region with a depth of around 1.5 $\mu$m, and it is not uniformly distributed in this region. It explains the higher hardness values for the specimen surface at 400 °C than those at 200 °C in Fig. 5(a). The results in Figs. 5 and 6 indicate that the ORL is very thin for the specimens tested at 200 °C and 400 °C in this study.

### *3.3.2. Internal crack initiation mechanism at room and high temperatures*

After the discussion on surface ORL and hardness of the specimens, the microstructure characteristics in the internal crack initiation zones and corresponding initiation mechanisms at room and high temperatures (400 °C) are concerned. Fig. 7(a) shows the rough area of the sample tested at 25 °C in Fig. 3(b3), and the sectional sheets at locations b and c were extracted. Fig. 7(b) is an SEM image of the sectional plane at position b in Fig. 7(a) and longitudinal $\alpha$ grains are found at the fracture surface. Fig. 7(c-e) give the IPF, phase map and TEM image of the sectional sheet at position c in Fig. 7(a), respectively. They present a long $\alpha$ grain along the fracture surface and this grain has been separated into many small grains and nanograins. The small grains and nanograins are discontinuously distributed along the surface, and they tend to be at some local positions but become few at other locations. Fig. 7(f) is the dark field view for the nanograins in box 1 in Fig. 7(e), and the selected area diffraction (SAD) in the figure shows many tiny dots placed in a ring pattern, which also suggests a polycrystalline structure consisting of refined grains. The grain refinement could be caused by dislocation interaction due to strain localization during the cyclic loading process [27, 42]. A similar phenomenon was also observed for an additively manufactured Ti-6Al-4V with basketweave microstructure [27]. When the sight moves to the microstructure below the nanograins in Fig. 7(c-e) and (g), it is clear that the large $\alpha$ grains and $\beta$-phase matrix are relatively intact with less deformation, although some dislocations are found in $\alpha$ grains in Fig. 7(g). It means that the deformation is locally nonuniform due to the microstructure inhomogeneity during cyclic loadings.

The microstructure characteristics of the internal crack initiation zone formed at 400 °C are shown in Fig. 8. A sectional sheet at position c in Fig. 8(a) has been extracted by FIB. Fig. 8(b) presents an SEM image of the sectional plane at position b in Fig. 8(a), and longitudinal $\alpha$ grains are located at the fracture surface. Fig. 8(c-e) shows the IPF, phase map and TEM image of the extracted sheet and lamellar $\alpha$ grains are laid at the observed surface in these figures. The nanograins are just observed in the $\alpha$ grains at the fracture surface, as shown in Fig. 8(c) and (d). Fig. 8(f) is the dark field view for the polycrystalline structure on the small hill in Fig. 8(e), and SAD pattern on the small hill in Fig. 8(f) also shows a diffused ring pattern, which indicates that nanograins are gathered at this area. The grain refinement process at 400 °C should be similar to that explained for room temperature [27]. When $\beta$ phases below the fracture surface are concerned in Fig. 8(c) and (d), it is found that, different from the relatively intact condition at 25 °C, the $\beta$ matrix at 400 °C shows obvious deformation with low resolution

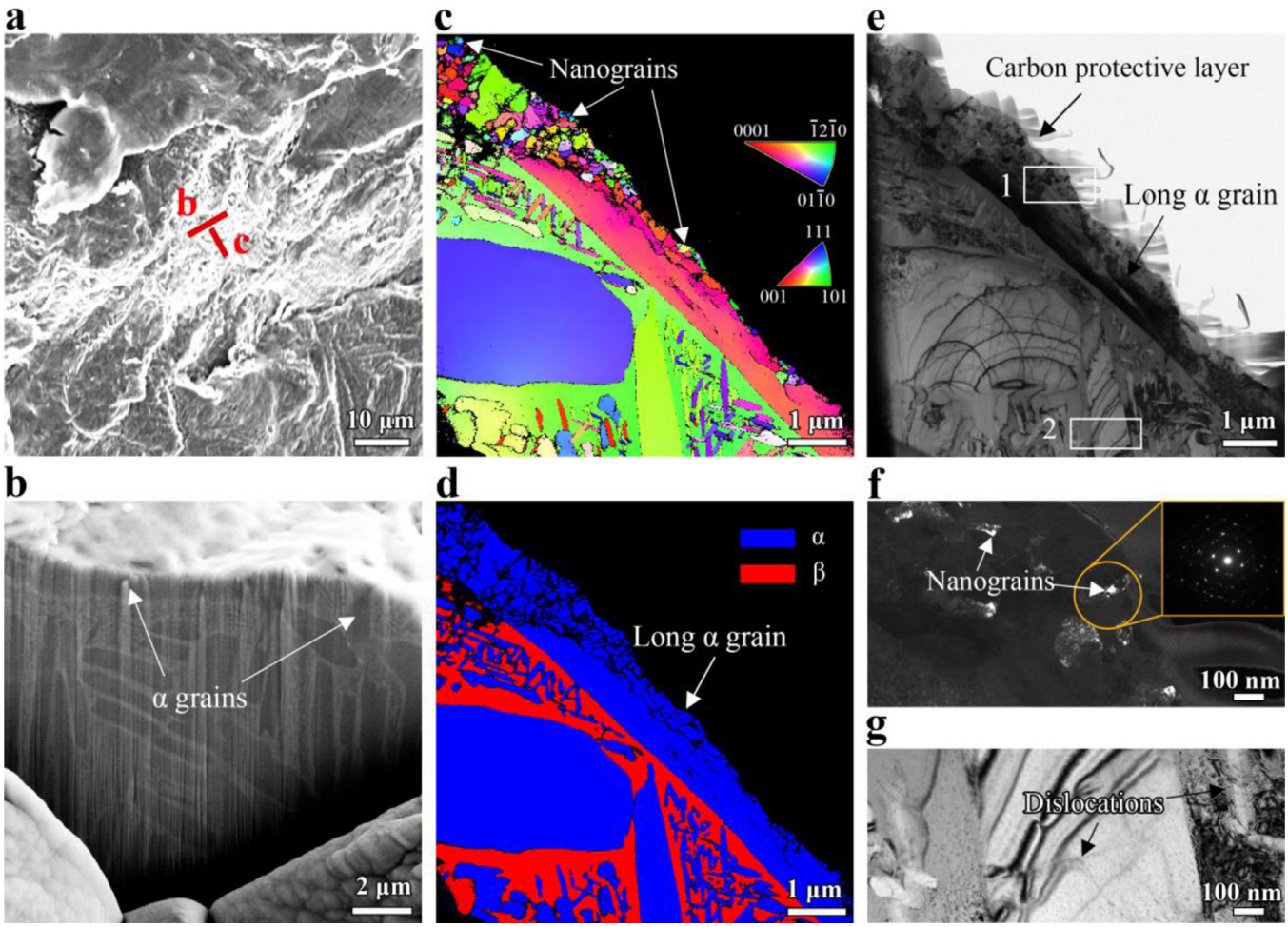


**Fig. 7.** Observations for the rough area of the sample tested at 25 °C ($\sigma_a$=620 MPa, $N_f$=6.0 × $10^6$ cycles). (a) SEM image of the rough area. (b) SEM image of the sectional plane at position b in (a). (c-e) IPF, phase map and TEM image of the sectional plane at position c in (a). (f) Dark field image and SAD of box 1 in (e); (g) An enlarged image of box 2 in (e).

in IPF and phase map. Additionally, in Fig. 8(g), more dislocations are found in $\alpha$ grains below the fracture surface. These figures indicate that the microstructure below the rough area experienced more severe deformation at 400 °C than those at 25 °C. Since the resistance to the dislocation movement of TC17 is reduced at 400 °C [4], it is reasonable to find more dislocations and deformation in $\alpha$ and $\beta$ phases around the rough area.

The competition mechanism between surface and interior crack initiation at 400 °C is shown in Fig. 9 and it should be related to surface ORL and dislocation movement in internal $\alpha$ grains at high temperature. On the one hand, the surface of the specimen became harder due to the ORL formed at 400 °C, which could restrain the surface crack initiation. The internal microstructure behaved with low dislocation resistance at 400 °C. The slip or strain localization in the microstructure could induce the internal crack initiation. On the other hand, the brittle fracture of oxygen-rich site or oxide shedding could occur at the surface and induce the crack initiation due to local stress concentration, as shown in Fig. 9(a1) and (b1). Therefore, when the fatigue life of the specimen by internal crack initiation was shorter than that by surface crack initiation, the internal failure mode would occur and vice versa. According to the results in Fig. 2(a), both the surface and internal failure modes could happen in fatigue life of $10^5$-$10^6$ cycles, but the internal failure mode became a major mode in the range $>10^6$ cycles. This indicates that the ORL tends to restrain the crack nucleation at the surface under a relatively low stress amplitude (i.e., longer fatigue life), and results in the internal crack initiation.

*3.3.3. Fatigue damage of notched specimens*

Fracture surface morphology of the notched specimens in Fig. 4 presented the crack initiation at notch root and this failure mode was commonly viewed for such specimens. Apart from SEM observation for those fractured specimens, some run-out specimens at different temperatures were cut along the loading direction to investigate the crack initiation or fatigue damage at the notch root. A specimen with the notch depth of 0.5 mm tested under a stress amplitude of 84 MPa at 25 °C was chosen and the band contrast map and IPF at the notch root are shown in Fig. 10(a) and (b), respectively. Fig. 10(c) and (d) present the band contrast map and IPF of a specimen with the notch depth of 0.2 mm and tested under a stress amplitude of 142 MPa at 200 °C. The band contrast maps of the two specimens presented that the crack initiated at the notch root and propagated for a length. According to the crack paths in the IPFs of Fig. 10(b) and (d), the cracks extended along or through the $\alpha$ grains. The crack paths were tortuous in the microstructure and this crack feature was common for the specimens in this study. These cracks in the specimens after fatigue loadings of 2.0 × $10^7$ cycles reveal an ultra-slow propagation process, and they might develop to be main cracks in VHCF regime. The specimen shown in Fig. 10(e) and (f) has a notch depth of 0.5 mm and was tested under a stress amplitude of 86 MPa at 400 °C for 5.0 × $10^7$ cycles. The notch depth of this specimen was the same as that at 25 °C in Fig. 10(a) and (b), and the stress amplitude was slightly higher. However, unlike the specimen at 25 °C, there is no obvious crack found in the SEM image of Fig. 10(e), and only some

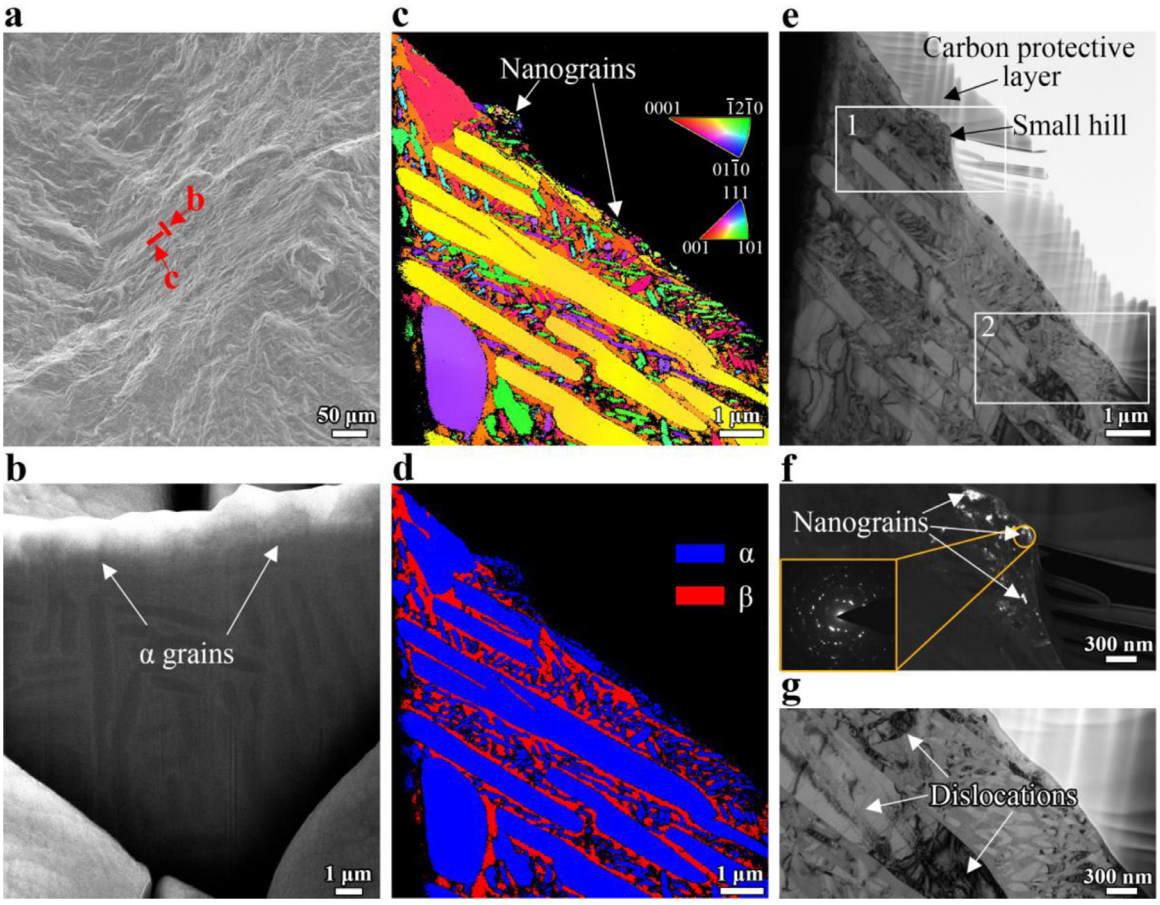


**Fig. 8.** Observations for the rough area of the sample tested at 400 °C ($\sigma_a$=520 MPa, $N_f$=1.0 × $10^6$ cycles). (a) SEM image of the rough area. (b) SEM image of the sectional plane at position b in (a). (c-e) IPF, phase map and TEM image of the sectional sheet at position c in (a). (f) Dark field image and SAD of box 1 in (e). (g) An enlarged image of box 2 in (e).

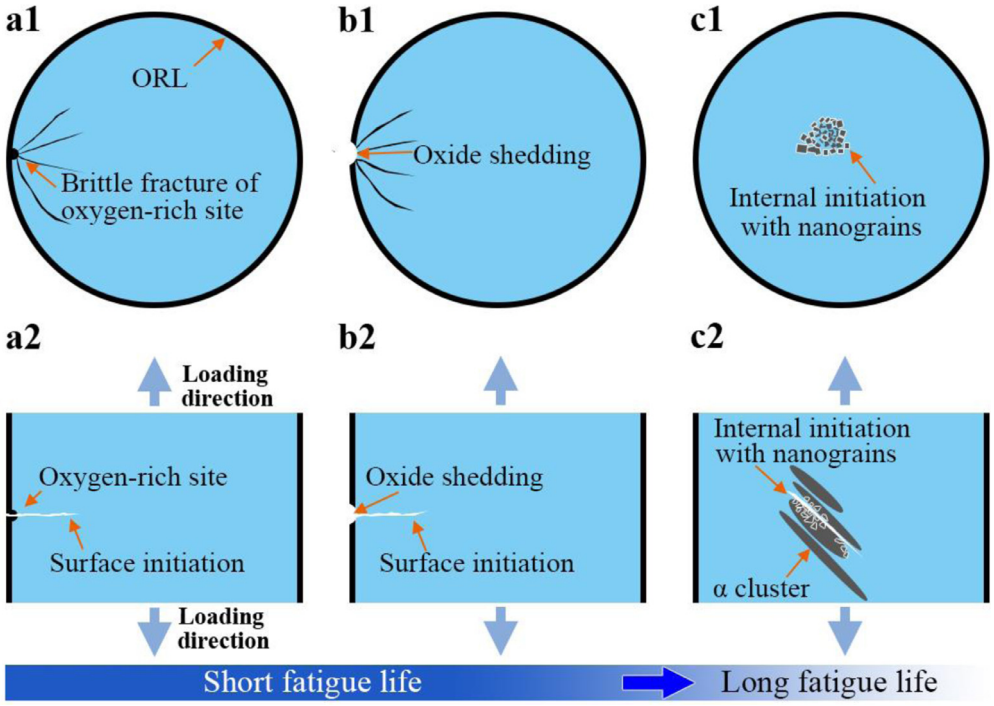


**Fig. 9.** Competition mechanism between surface and internal initiations at 400 °C. (a1) and (a2) Section view and side view of surface crack initiation by brittle fracture of oxygen-rich site, respectively. (b1) and (b2) Section view and side view of surface crack initiation by oxide shedding, respectively. (c1) and (c2) Section view and side view of internal crack initiation with rough area, respectively.

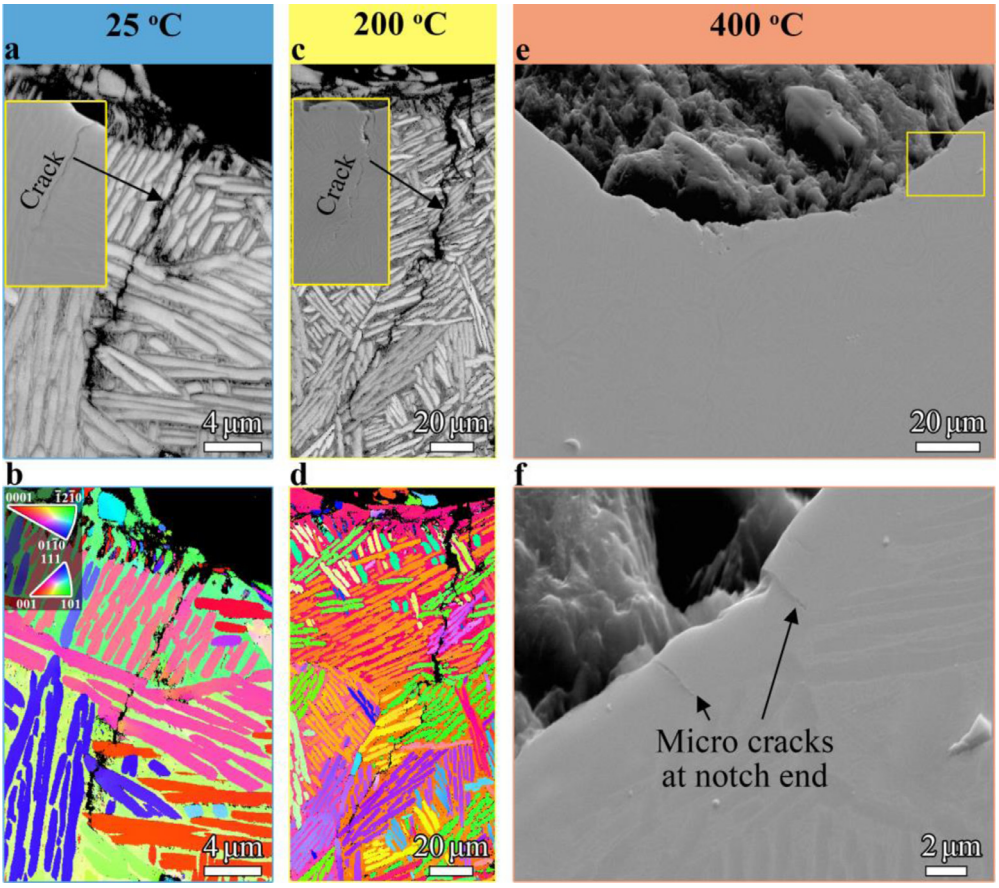


**Fig. 10.** Cracks below the notch defect. (a) and (b) Band contrast map and IPF of a specimen with the notch depth of 0.5 mm tested at 25 °C. Inset in (b) the color legend of IPF. (c) and (d) Band contrast map and IPF of a specimen with the notch depth of 0.2 mm tested at 200 °C. Inset in (a) and (c) SEM images of cracks in (a) and (c), respectively. (e) SEM image of a specimen with the notch depth of 0.5 mm tested at 400 °C. (f) An enlarged view of yellow box in (e).

micro cracks exist around the notch root in Fig. 10(f). It might be attributed to the hardened ORL formed at the notch root at the high temperature which inhibited the crack propagation. The effect of ORL has been discussed in the competition mechanism in Section 3.3.1. The finding in Fig. 10(e) and (f) further suggests that the hardened ORL could suppress surface crack initiation under a low stress amplitude even after $5.0 \times 10^7$ cyclic loadings.

### 3.4. Fatigue strength modeling

According to Fig. 2(b), the relation for fatigue strength of smooth specimens $\sigma_{fs0}$ and temperature $t$ could be expressed as follows:

$$\sigma_{fs0} = A - Bt \quad (1)$$

where $A$ and $B$ are fitting coefficients and they are determined to be $A$=643 MPa and $B$=0.567 MPa/°C, temperature $t$ has been validated in a range of 25 °C to 400 °C in this study.

To establish a fatigue strength model for the specimens with small defects (i.e., small notches), the fatigue strengths corresponding to the defect sizes are plotted as solid symbols in Fig. 11 in a log-log scale. The fatigue strengths of smooth specimens at 25 °C, 200 °C and 400 °C are labeled with hollow symbols, the horizontal coordinate of which are taken as around 1 $\mu$m in Fig. 11. Defect sizes were determined by $\sqrt{\text{area}}$, where *area* was the projection area of the defect perpendicular to the principal stress. The parameter $\sqrt{\text{area}}$ was proposed by Murakami [43] to correlate the fatigue strength and defect size at room temperature and it has been widely used for the influence of defect in literature

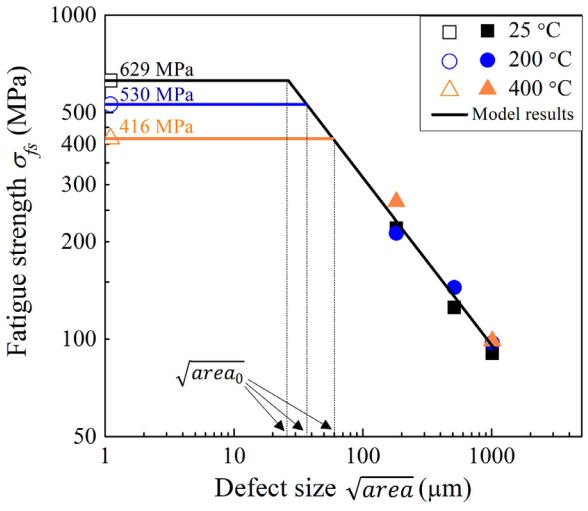


**Fig. 11.** Variation of fatigue strength with defect size. Hollow symbols and solid symbols in the figure represent experimental fatigue strengths of smooth specimens and notched specimens, respectively.

[28, 29, 31, 44]. The current study expanded its application in the present material at high temperatures. Defect size $\sqrt{\text{area}}$ for different depths of notches are shown in Table 3, which are calculated through the notch depths and the radius of the smallest section of the specimens. It is seen from Fig. 11 that the experimental fatigue strengths of notched specimens at 25 °C and 200 °C are re-

**Table 3**
The notch depth and defect size $\sqrt{area}$ of notched specimens.

| Depth (mm) | $\sqrt{area}$ ($\mu$m) |
|---|---|
| 0.05 | 182 |
| 0.2 | 513 |
| 0.5 | 1011 |

duced with larger defect sizes and the decrease trends of fatigue strengths at both temperatures are similar. The notched specimens with a defect size of 182 $\mu$m at 400 °C present a higher fatigue strength than those at 25 °C and 200 °C. At a defect size of 1011 $\mu$m, the fatigue strengths at different temperatures are close. Generally, the temperature effect on the fatigue strength of notched specimens was minor and the defect size dominated its performance.

Based on the experimental results in Fig. 11, the fatigue strength $\sigma_{fs}$ incorporating both the temperature and the defect size could be expressed as follows:

$$\log_{10}\sigma_{fs} = \begin{cases} \log_{10}\sigma_{fs0}, \ 0 \le \sqrt{area} \le \sqrt{area_0} \\ -n\log_{10}\sqrt{area} + \log_{10}C, \ \sqrt{area} > \sqrt{area_0} \end{cases} \quad (2)$$

where $n$ and $C$ are fitting coefficients, $\sqrt{area_0}$ denotes the critical size of defect less than which the defect does not affect the fatigue strength and it is determined by $\sqrt{area_0} = 10^{\left(\frac{\log_{10}C - \log_{10}\sigma_{fs0}}{n}\right)}$.

Substituting Eq. (1) in Eq. (2), a fatigue strength model is obtained as Eq. (3):

$$\log_{10}\sigma_{fs} = \begin{cases} \log_{10}(A - Bt), \ 0 \le \sqrt{area} \le \sqrt{area_0} \\ -n\log_{10}\sqrt{area} + \log_{10}C, \ \sqrt{area} > \sqrt{area_0} \end{cases} \quad (3)$$

In this study, coefficients $n$ and $C$ are fitted by the fatigue strength associated with the defect size at different temperatures, and the results indicate weak dependence of the fatigue strength of notched specimens on the temperature. The values of $n$ and $C$ are determined to be 0.518 and 3418, respectively. The model results are shown in Fig. 11, and they correlate well with the experimental fatigue strengths for the range of the present test conditions. Fig. 11 also indicates that the critical defect size is increased at high temperatures. It might be attributed to surface hardened oxide which could restrain the crack nucleation.

## 4. Conclusion

The high-temperature fatigue behavior and failure mechanism of TC17 alloy have been investigated in HCF and VHCF regimes. A new failure mechanism was observed for titanium alloy at high temperature in HCF regime. Additionally, the notched specimens were examined at room and high temperatures to study the coupled effect of temperature and defect on the fatigue behavior of TC17 alloy. Based on these results and analysis, the main conclusions of this study are as follows:

(1) The tensile strength and fatigue strength of smooth specimens decreased with an increase of temperature. The ratios of the fatigue strength to the tensile strength were distributed in a range of 0.46 to 0.55. However, the fatigue strengths of the notched specimens were not sensitive to the temperatures but the defect size.

(2) Three failure mechanisms were found for the smooth specimens at 400 °C, including brittle fracture of surface oxygen-rich site, oxide shedding induced fracture, and internal crack induced fracture. The competition between surface and internal crack initiations was noticed in HCF regime. At a high stress amplitude, both surface and internal crack initiations could happen. When the stress amplitude was lower and the fatigue life was longer, the hardened surface might not fracture. The internal microstructure showed lower resistance to dislocation at high temperatures, and the slip or strain localization could nucleate cracks at the interior of specimens.

(3) The failure mechanism of the notched specimens was not affected by the temperature and the specimens failed by cracks initiating from the notch root. It could be attributed to that the stress concentration at the notch root resulted in initial cracks and this failure mode remained at room and high temperatures.

(4) A linear relation was found between the fatigue strength of smooth specimens and the temperatures in the range of 25 °C to 400 °C. Based on this relation and $\sqrt{area}$ parameter, a fatigue strength model considering the coupled effect of temperature and defect was proposed for smooth and notched specimens. The model has been validated in the range of the present test conditions.

## Declaration of Competing Interest

The authors declare that they have no known competing financial interests or personal relationships that could have appeared to influence the work reported in this paper.

## Acknowledgement

This work was financially supported by the National Natural Science Foundation of China (No. 91860112) and the International Postdoctoral Exchange Fellowship Program (China).

## References

[1] S. Hardt, H. Maier, H. Christ, Int. J. Fatigue 21 (1999) 779–789.
[2] D.P. Satko, J.B. Shaffer, J.S. Tiley, S.L. Semiatin, A.L. Pilchak, S.R. Kalidindi, Y. Kosaka, M.G. Glavicic, A.A. Salem, Acta Mater 107 (2016) 377–389.
[3] K. Tokaji, Scr. Mater. 54 (2006) 2143–2148.
[4] F. Liu, Y. Chen, C. He, L. Li, C. Wang, H. Li, H. Zhang, Q. Wang, Y. Liu, Mater. Sci. Eng. A 811 (2021) 141049.
[5] H. Christ, F. Fischer, H. Maier, Mater. Sci. Eng. A 319 (2001) 625–630.
[6] G. Biallas, M. Essert, H. Maier, Int. J. Fatigue 27 (2005) 1485–1493.
[7] D. Eylon, M. Rosenblum, Metall. Trans. A 13 (1982) 322–324.
[8] W. Plumbridge, Fatigue Fract. Eng. Mater. Struct. 10 (1987) 385–398.
[9] G. Malakondaiah, T. Nicholas, Metall. Mater. Trans. A 27 (8) (1996) 2239.
[10] V. Recina, B. Karlsson, Mater. Sci. Eng. A 262 (1999) 70–81.
[11] V. Recina, Mater. Sci. Technol. 16 (2000) 333–340.
[12] J. Cao, F. Bai, Z. Li, Mater. Sci. Eng. A 424 (2006) 47–52.
[13] F. Appel, T.K. Heckel, H. Christ, Int. J. Fatigue 32 (2010) 792–798.
[14] I. Altenberger, R.K. Nalla, Y. Sano, L. Wagner, R.O. Ritchie, Int. J. Fatigue 44 (2012) 292–302.
[15] P. Gallo, F. Berto, P. Lazzarin, Theor. Appl. Fract. Mech. 76 (2015) 27–34.
[16] H. Ghonem, Int. J. Fatigue 32 (2010) 1448–1460.
[17] G. Qian, Z. Jian, X. Pan, F. Berto, Int. J. Fatigue 133 (2020) 105424.
[18] Y. Hong, C. Sun, Theor. Appl. Fract. Mech. 92 (2017) 331–350.
[19] H. Su, X. Liu, C. Sun, Y. Hong, Fatigue Fract. Eng. Mater. Struct. 40 (2017) 979–993.
[20] X. Pan, H. Su, C. Sun, Y. Hong, Int. J. Fatigue 115 (2018) 67–78.
[21] X. Liu, C. Sun, Y. Hong, Mater. Sci. Eng. A 622 (2015) 228–235.
[22] X. Liu, C. Sun, Y. Hong, Int. J. Fatigue 92 (2016) 434–441.
[23] C. Huang, Y. Zhao, S. Xin, C. Tan, W. Zhou, Q. Li, W. Zeng, Mater. Sci. Eng. A 682 (2017) 107–116.
[24] C. Huang, Y. Zhao, S. Xin, C. Tan, W. Zhou, Q. Li, W. Zeng, Int. J. Fatigue 94 (2017) 30–40.
[25] E. Takeuchi, Y. Furuya, N. Nagashima, S. Matsuoka, Fatigue Fract. Eng. Mater. Struct. 31 (2008) 599–605.
[26] X. Pan, S. Xu, G. Qian, A. Nikitin, A. Shanyavskiy, T. Palin-Luc, Y. Hong, Mater. Sci. Eng. A 798 (2020) 140110.
[27] C. Sun, W. Chi, W. Wang, Y. Duan, Int. J. Mech. Sci. 205 (2021) 106591.
[29] M. Filippini, S. Beretta, L. Patriarca, G. Pasquero, S. Sabbadini, Procedia Eng 10 (2011) 3677–3682.
[30] M. Filippini, S. Beretta, L. Patriarca, G. Pasquero, S. Sabbadini, J. ASTM Int. 9 (2012) 1–12.
[31] M. Ding, Y. Zhang, H. Lu, Int. J. Fatigue 139 (2020) 105793.
[32] J. Wang, W. Peng, J. Yu, J. Wang, M. Ding, Y. Zhang, Mater. Sci. Technol. 37 (2021) 301–313.
[33] M. Nazmy, M. Staubli, G. Onofrio, V. Lupinc, Scr. Mater. 45 (2001) 787–792.
[34] Standard Practice for Conducting Force Controlled Constant Amplitude Axial Fatigue Tests of Metallic Materials, ASTM Int., West Conshohocken, PA, 2015.

[35] C. Sun, Q. Song, Metals 8 (2018) 811.
[36] Y. Hong, A. Zhao, G. Qian, Acta Metall. Sin. 45 (2009) 769–780 (in Chinese).
[37] Z. Huang, H. Liu, H. Wang, D. Wagner, M. Khan, Q. Wang, Int. J. Fatigue 93 (2016) 232–237.
[38] J.C. Stinville, E. Martin, M. Karadge, S. Ismonov, M. Soare, T. Hanlon, S. Sundaram, M.P. Echlin, P.G. Callahan, W.C. Lenthe, Acta Mater 152 (2018) 16–33.
[39] A. Cervellon, J. Cormier, F. Mauget, Z. Hervier, Y. Nadot, Metall. Mater. Trans. A 49 (2018) 3938–3950.
[40] H. Kobayashi, A. Todoroki, T. Oomura, T. Sano, T. Takehana, Int. J. Fatigue 28 (2006) 1633–1639.
[41] M. Zhu, F. Xuan, Y. Du, S. TuInt, J. Fatigue 40 (2012) 74–83.
[42] C. Sun, Q. Song, L. Zhou, J. Liu, Y. Wang, X. Wu, Y. Wei, Int. J. Fatigue 124 (2019) 483–492.
[43] Y. Murakami, Metal fatigue: effects of small defects and nonmetallic inclusions, Academic Press, 2019.
[44] W. Chi, W. Wang, W. Xu, G. Li, X. Chen, C. Sun, Eng. Fract. Mech. 259 (2021) 108136.